Inversion of Hyperpolarized 13 C NMR Signals through Cross-Correlated Cross-Relaxation in Dissolution DNP Experiments

Mattia Negroni, David Guarin, Kateryna Che, Ludovica M Epasto, Ertan Turhan, Albina Selimović, Fanny Kozak, Samuel Cousin, Daniel Abergel, Geoffrey Bodenhausen, et al.

Inversion of Hyperpolarized ^{13}C NMR Signals Through Cross-Correlated Cross-Relaxation in Dissolution DNP Experiments

Mattia Negroni[1], David Guarin[2,3], Kateryna Che[1], Ludovica M. Epasto[1], Ertan Turhan[1], Albina Selimović[1], Fanny Kozak[1], Samuel Cousin[4], Daniel Abergel[5], Geoffrey Bodenhausen[5], Dennis Kurzbach[1,]*

[1] *University Vienna, Faculty of Chemistry, Institute of Biological Chemistry, Währinger Str. 38, 1090 Vienna, Austria*

[2] *Athinoula A. Martinos Center for Biomedical Imaging, Department of Radiology, Massachusetts General Hospital, Charlestown, Massachusetts 02129, USA*

[3] *Polarize ApS, 1808 Frederiksberg, Denmark*

[4] *Institut de Chimie Radicalaire - UMR 7273, Saint-Jérôme Campus, Av. Esc. Normandie Niemen, Aix-Marseille Université / CNRS, 13397 Marseille, Cedex 20, France*

[5] *Laboratoire des Biomolécules, LBM, Département de chimie, École Normale Supérieure, PSL University, Sorbonne Université, CNRS, 24 rue Lhomond, 75005 Paris, France*

[*] *E-mail: dennis.kurzbach@univie.ac.at*

ABSTRACT

Dissolution dynamic nuclear polarization (DDNP) is a versatile tool to boost signal amplitudes in solution-state nuclear magnetic resonance (NMR) spectroscopy. For DDNP, nuclei are spin-hyperpolarized '*ex-situ*' in a dedicated DNP device and then transferred to an NMR spectrometer for detection. Dramatic signal enhancements can be achieved, enabling shorter acquisition times, real-time monitoring of fast reactions, and reduced sample concentrations. Here we show how this transfer can affect NMR spectra through cross-correlated cross-relaxation (CCR), especially in the case of low-field passages. Such processes can selectively invert signals of ^{13}C spins in proton-carrying moieties. For their investigations, we use schemes for simultaneous or 'parallel' detection of hyperpolarized ^{1}H and ^{13}C nuclei. We find that $^{1}H_{\sqcup}{}^{13}C$ CCR can invert signals of ^{13}C spins if the proton polarization is close to 100%. We deduce that low-field passage in a DDNP experiment, a common occurrence since the introduction of so-called 'ultra-shielded´ magnets, accelerates these effects due to field-dependent paramagnetic relaxation enhancements that can influence CCR, ^{13}C spins not coupled to nearby protons do not feature any inversion phenomena. The reported effects are demonstrated for various molecules, laboratory layouts, and DDNP systems. As coupled ^{13}C-^{1}H spin systems are ubiquitous, we expect these effects to be observed in various DDNP experiments. This might be exploited for selective spectroscopic labeling of hydrocarbons.

INTRODUCTION

Recent years have witnessed an increasing interest in so-called hyperpolarization techniques that enable the detection of nuclear magnetic resonance (NMR) signals with significantly enhanced intensities.[1-2] Hyperpolarization techniques provide the potential to overcome some of the limitations imposed by the intrinsically weak signals detected in conventional NMR spectroscopy. Signal enhancements of up to four orders of magnitude allow one to reduce acquisition times and sample concentrations.

In particular, the development of dissolution dynamic nuclear polarization (DDNP)[3-6] has significantly stimulated recent uses of hyperpolarized NMR. Applications have been found, for example, in NMR of proteins[7-11], ligand binding studies[12-14], metabolomics[15-17], interaction monitoring[18-19], NMR of long-lived states[20-22], and metabolic imaging[23-27]. The commercialization of DDNP equipment has further helped to popularize this technique.[28]

For DDNP, a target molecule can be hyperpolarized '*ex-situ*' in a dedicated apparatus that enables microwave irradiation of paramagnetically doped samples at low temperatures (close to 1 K) and in high magnetic fields (typically >3 T). After build-up of the hyperpolarization, the sample is dissolved (typically with a burst of superheated D_2O) and transferred to an NMR spectrometer for NMR detection in the liquid state. One critical criterion that needs to be fulfilled by the target molecules is that longitudinal relaxation times should be long enough to allow for sample transport from the DNP system to the NMR spec-

trometer – a process that typically takes 1 to 5 s depending on the experimental setup.

The magnetic field along the transfer path of the sample depends critically on the layout of the laboratory.[29-31] Stray fields of different magnets may not be known accurately. This is particularly true for stray fields near the bore openings of shielded NMR magnets, where the fields may be entirely canceled or even undergo a reversal.

Here we report unexpected effects on spectra detected in dissolution DNP experiments. We demonstrate how *cross-correlated cross-relaxation* (CCR) between hyperpolarized protons and adjacent carbon-13 nuclei can lead to ^{13}C signal inversion. Such effects cannot be observed in conventional thermal equilibrium NMR. However, they dominate NMR spectra when proton polarizations reach values larger than several tens of percent in solution, which is often the case in DDNP experiments. Furthermore, such effects are boosted during low-field transfer passages due to the presence of paramagnetic molecules in the dissolved sample.

We have observed these effects in experiments performed on two entirely different DDNP systems installed in two different laboratories in Vienna and Paris. In addition, we have probed such hyperpolarized CCR effects using two different samples; namely, pyruvate-1-^{13}C dissolved in ethylene glycol (EG) and methanol mixed with glycerol-d_8.

METHODS

All DDNP experiments were performed with 2-stage setups, where the sample is hyperpolarized in a separate DNP system and then dissolved and transferred to an NMR spectrometer for detection. In all cases, the samples traveled through magnetic tunnels that provided a magnetic field B_{Tunnel} > 0.5 T between the DNP magnet and the NMR spectrometer. In the Vienna set-up, both ends of the tunnels[29] were suspended ca. 30 cm above the bores of the polarizer and NMR magnets. Between the polarizer and the entrance to the tunnel, a pulsed solenoidal magnet[32] has been used in some experiments providing a field of $B_{Solenoid}$ > 0.2 T. Likewise, the space between the exit from the tunnel and the entrance of the bore of the NMR magnet could be bridged by a pulsed solenoid[32] if desired. The pulsed solenoids ended ca. 5 cm before the bore of the magnets. In the Paris set-up, the polarizer end of the tunnel was somewhat farther from the magnet bore (~70 cm), and no additional solenoid was used.

Sample Preparation. For one sample type, 500 mM of ^{13}C1 labeled pyruvate, and 40 mM TEMPOL were dissolved in a 5:4:1 mixture of EG, D_2O, and H_2O. For the second sample type, methanol-OD was mixed 1:1 with glycerol-d_8 with 15 mM TEMPOL.

Dissolution DNP. In Vienna, the dissolution DNP experiments were performed as described in reference [32]. In brief, 100 μL of a paramagnetically doped methanol/glycerol sample was hyperpolarized for 1 h at 1.4 K in a magnetic field of $B_{0,DNP}$ = 6.7 T either positively at a microwave frequency of 188.08 GHz or negatively at a frequency 188.4 GHz. Dissolution was performed with 5 mL D_2O at 15.0 bar and 240˚ C. The transfer of the dissolved hyperpolarized liquid to the NMR spectrometer took 4 s. The ^{1}H and ^{13}C signals were detected simultaneously once per second on a Bruker NEO 500 MHz spectrometer equipped with a BBFO Prodigy cryogenic probe head, using 1° and 30° flip angles, respectively. The setup is sketched in Fig. 1.

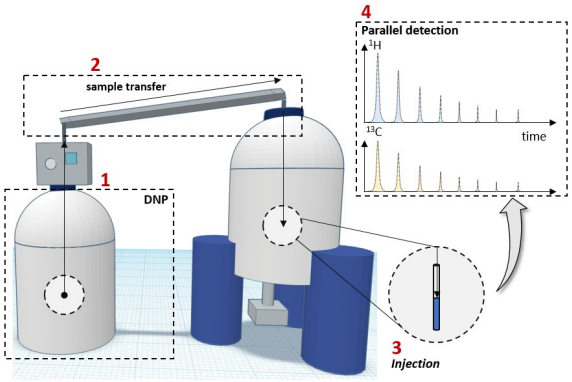

Figure 1. Schematic dissolution DNP. The samples are hyperpolarized at low temperatures in a dedicated DNP magnet (1) before being (2) dissolved and pneumatically propelled to an NMR spectrometer, where (3) the sample is injected for detection into an NMR tube (4). The hyperpolarization can be detected simultaneously ('in parallel') on the ^{1}H and ^{13}C channels using multiplexed receiver technology.

In Paris, DDNP experiments were performed on a Bruker prototype operating at 6.7 T and 1.2 K. Again, 50 μL of a paramagnetically doped sample was used. In contrast to the experiments in Vienna, ^{13}C hyperpolarization was boosted by ^{1}H-^{13}C cross-polarization.[33] The optimal amplitude of the spin-locking ^{13}C radiofrequency field was $\gamma B_1/(2\pi)$ = 50 kHz, and the duration of the Hartmann-Hahn contact was 0.4 < τ_{SL} < 0.5 s. A gated μW field[34] with a power of 350 mW at 188.4 GHz, modulated with a 100 MHz amplitude saw-tooth function with a modulation frequency of 2 kHz, was used to saturate part of the EPR spectrum of the free radicals. Dissolution and transfer to the detection NMR spectrometer were performed with 5 mL D_2O at 10.5 bar and 180˚ C. The transfer of the dissolved hyperpolarized liquid to the NMR spectrometer took 5 s. The ^{13}C signals were detected on a Bruker 400 MHz spectrometer using a 10 mm BBO broadband probe at room temperature. Pulses with 10˚ angles were applied only to ^{13}C at intervals of 1 s.

The magnetic fields between the DNP and the NMR systems in Vienna were measured with a Hirst GM08 Gauss meter.

Simulations. All simulations were carried out with the SpinDynamica[35] Software package for Mathematica (time dependence of the magnetization), RedKite[36] (Relaxation matrices), or a home-written script in Matlab (field-dependence of paramagnetic relaxation rates). All codes and scripts can be downloaded (see the Code Availability section). Multiplet intensities have been fitted using the MATLAB-based 'fitnlorentzian.m' function. The most critical simulation codes are furthermore shown explicitly in the Supporting Information.

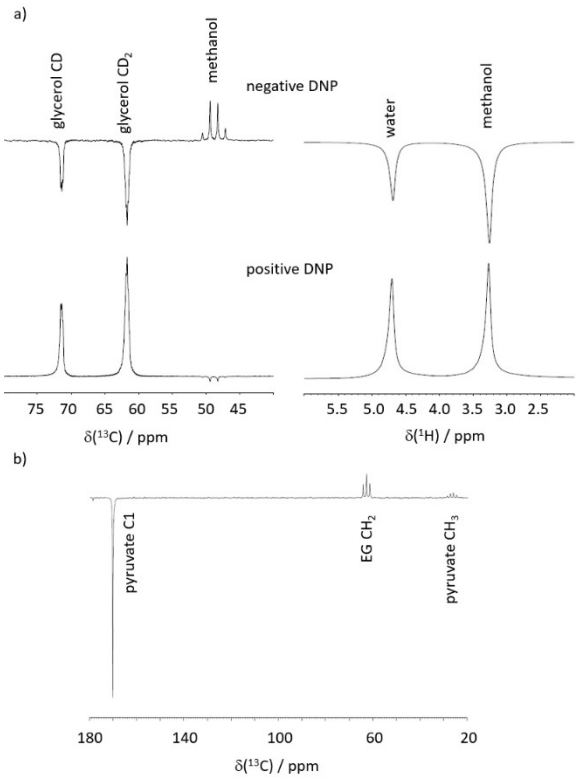

Fig. 2a shows ^{1}H and ^{13}C spectra for the methanol/glycerol-d_8 mixture detected in parallel after the dissolution of positively (bottom) or negatively (top) hyperpolarized samples. All ^{1}H and ^{13}C signals of glycerol-d_8 show positive and negative amplitudes as expected. However, the ^{13}C-methanol signals have opposite amplitudes. The signal enhancements ε for methanol are similar or weaker ($\varepsilon \approx -3200$ for positive and $\varepsilon \approx +400$ for negative DNP) than those of glycerol-d_8 ($\varepsilon \approx +7600$ and -1700, respectively).

Fig. 2b displays similar results for the pyruvate/EG mixture. After negative DNP, dissolution, and transfer, the 1-^{13}C NMR signal of pyruvate is negative, as expected, while the pronated $^{13}CH_2$ signals of EG, as well as those of $^{13}CH_3$ in pyruvate, are inverted relative to those of pyruvate C1. Note the intense signal of the methyl group compared to C1 despite the selective labeling of the latter.

The signal enhancements obtained with negative DNP for pyruvate-^{13}C and EG were $\varepsilon \approx -19000$ and +14000, respectively.

THEORY

To discuss and analyze the signal inversion presented above, this section provides a brief overview of the spin physics underlying the $^{13}CH_2$ and $^{13}CH_3$ groups of ethylene glycol and methanol-OD.

Methylene $^{13}CH_2$ moieties. It is well known that two interacting degenerate protons generate 4 stationary nuclear spin states. Three of them constitute triplet states (T). In the Zeeman basis, these can be expressed as

$$|\alpha\alpha\rangle,\ (|\alpha\beta\rangle + |\beta\alpha\rangle)2^{-1/2} \text{ and } |\beta\beta\rangle \quad (1)$$

The fourth state is a singlet state (S), which we express as:

$$(|\alpha\beta\rangle - |\beta\alpha\rangle)2^{-1/2} \quad (2)$$

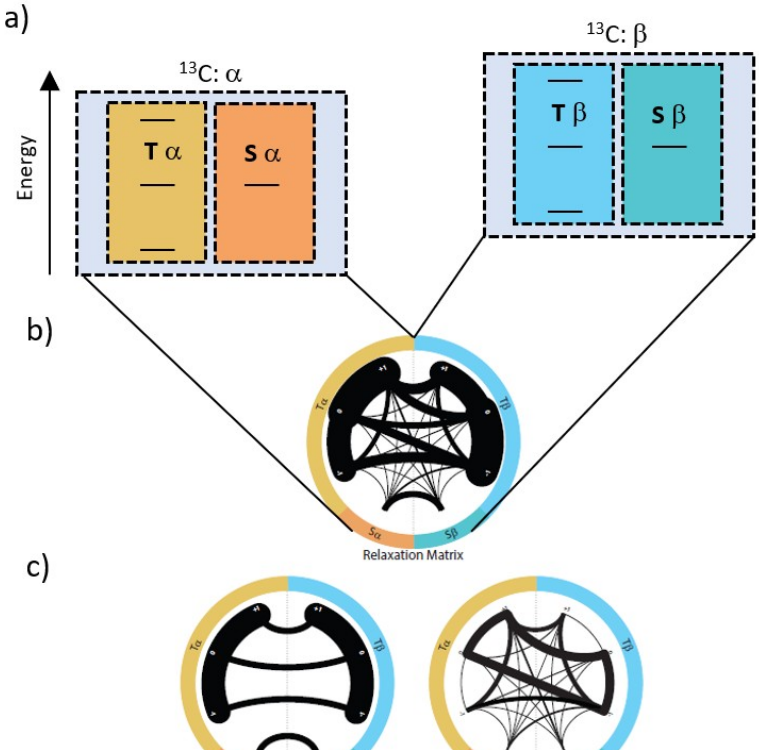

pointed out by Levitt and co-work-
by dipolar couplings or random field
veen the singlet and triplet manifolds
ıin the Redfield approach that corre-
d-order perturbation theory. For pro-
rbon spins, too), several relaxation
active - we here consider chemical
(CSA), dipole-dipole (DD) couplings,
erms, and random field relaxation
the dipolar and random field contri-
cally the strongest: if they are ne-
ations, this significantly prolongs the
equilibrium population imbalance be-
states. This population imbalance
equilibrium.[20, 38-39]

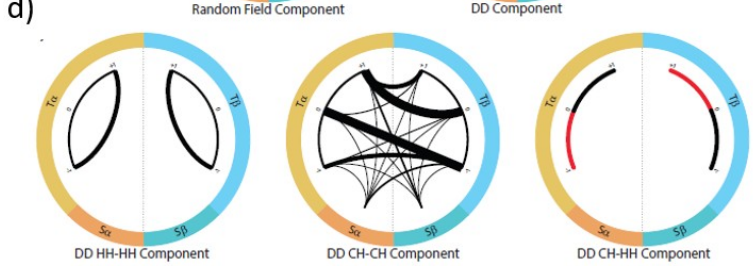

Figure 3. Graphical representation of $^{13}CH_2$ spin state levels a) Spin energy levels. b) Representation of the relaxation matrix (dipolar plus random field) elements connecting the different spin states. The spin states (energy levels) are represented on the outer ring (T and S states in orange and yellow). The left side corresponds to the α carbon-13 spin state, the right to the β state. Black lines connecting the states correspond to possible relaxation pathways. The thicker lines indicate higher rates and faster relaxation. Asymmetric, i.e., 'diagonal' relaxation pathways can convert proton polarization into carbon polarization. Hence, it becomes evident which contributions cause the reported signal inversion effect. c) Representation of the random field (rnd) relaxation matrix. d) Representation of various components of the DD relaxation matrix. Red indicates negative relaxation rates.

In the presence of a third interacting spin (carbon-13 in a $^{13}CH_2$ group) the two manifolds are split into four. Fig. 3a shows the resulting energy diagram. Importantly, the third spin enables a weak yet significant population flow between the S and T manifold due to DD CCR involving the dipoles between the central carbon and the two protons (denoted CH-CH DD in Figure 3).

To help the reader visualize the relaxation pathways, we developed a comprehensive representation of the different states and the flow of populations between them (Fig. 3b-d.) Note that the graphical representation refers to relaxation between populations of eigenstates. The different spin states are represented by the outer ring (triplet states on top, singlet states at the bottom). The ^{13}C spin mirrors the S and T states vertically, creating eight levels. The correlation to a more common representation is also shown. Panels 3b to 3d visualize the relaxation pathways as black lines between the levels; the thicker the line, the higher the relaxation rate. The relaxation rates have been computed using SpinDynamica by expressing the relaxation superoperator through standard semi-classical treatment of spin relaxation detailed in reference [21] (further details can be found in the Supporting Information).

Three important observations can be made: *(i)* Considering the entire relaxation matrix (Fig. 3b), it can be seen that the flow either within the triplet or the singlet manifold is much faster than the flow between them. *(ii)* Investigating the dipolar and random field relaxation mechanisms independently (Fig. 3c and 3d), we find that the random field contribution can efficiently relax protons and carbon spins. However, the flow between ^{13}C states is only possible when the ^{1}H state remains unchanged. Hence, proton polarization cannot directly relax into carbon polarization. (*iii*) DD CCR involving both carbons and protons can efficiently cause relaxation between two different ^{13}C states. But in contrast to random field relaxation, the ^{13}C relaxation pathway connects two different ^{1}H levels. Hence, proton polarization can be converted into carbon polarization. The difference between points (ii) and (iii) is reflected in Fig. 3 through the symmetry w.r.t. the vertical axis. Random field relaxation leads to a symmetric representation, while DD relaxation entails an asymmetric (diagonal) connection between the proton states on each site. The usefulness of the circular representation becomes evident: Only when these representations involve an asymmetric pathway that crosses the central vertical axis can polarization be transferred from a proton to a carbon nucleus or *vice-versa*.

It should be noted that the polarization transfer is more efficient (corresponding to thicker lines) within the triplet manifold than between the triplet and the singlet manifolds, which is expected, as this process is not symmetry forbidden. Hence longitudinal $^{1}H_z$ magnetization can be converted into $^{13}C_z$ polarization more efficiently than a singlet-triplet population imbalance. Furthermore, note that the ^{13}C polarization produced by CCR from ^{1}H spins shows an inverted sign due to the CH-CH DD pathway. This is again reflected in the fact that the relaxation pathway is not symmetric w.r.t. the central axis in Fig. 3. In other words, higher energy proton states are converted into lower energy carbon states and *vice-versa*. Hence, the polarization transfer involves a change in sign.

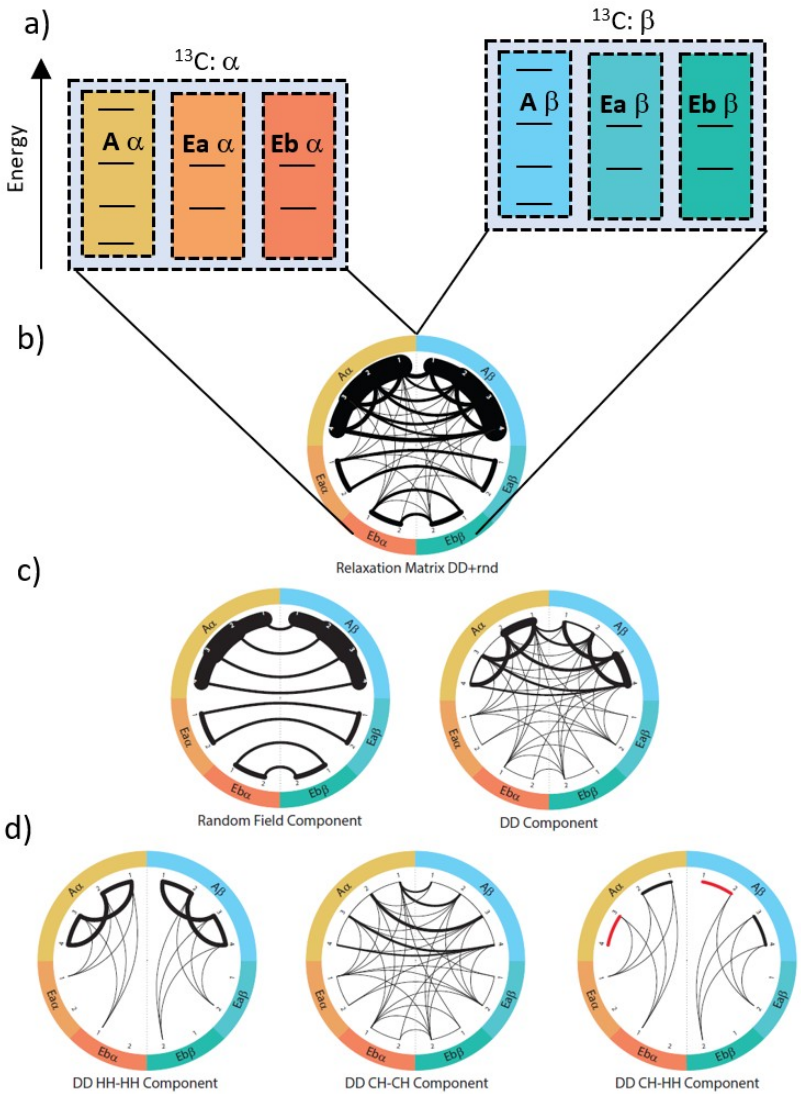

Figure 4. Graphical representation of $^{13}CH_3$ spin state levels: a) Spin energy levels. b) Representation of the relaxation matrix (dipolar plus random field) elements connecting the different spin states. The spin states (energy levels) are represented on the outer ring (A and E states in orange and yellow). The left side corresponds to the α carbon-13 spin state, the right to the β state. Black lines connecting the states correspond to possible relaxation pathways. The thicker lines indicate faster relaxation rates. Asymmetric, i.e., 'diagonal' relaxation pathways can convert proton polarization into carbon polarization. Hence, it becomes evident which contribution causes the reported signal inversion effect. c) Representation of the random field relaxation matrix. d) Representation of the various components of the DD relaxation matrix; red lines indicate negative values.

Methyl $^{13}CH_3$ moieties. The situation is more complex for a methyl group, as the C_{3v} symmetry and the additional proton need to be considered. However, similar reasoning as for the methylene group applies. The eight ^{1}H spins states can be grouped into manifolds of three irreducible representations, i.e., A, E_a, and E_b. Four states in the A manifold, two in E_a and another two in the E_b manifold:

A:

$$|\alpha\alpha\alpha\rangle,\ (|\alpha\alpha\beta\rangle + |\alpha\beta\alpha\rangle + |\beta\alpha\alpha\rangle)3^{-1/2},\ (|\alpha\beta\beta\rangle + |\beta\alpha\beta\rangle + |\beta\beta\alpha\rangle)3^{-1/2},\ |\beta\beta\beta\rangle \quad (3)$$

E_a:

$$(|\alpha\alpha\beta\rangle + e^{-i2\pi/3}|\beta\alpha\alpha\rangle + e^{i2\pi/3}|\alpha\beta\alpha\rangle)3^{-1/3},\ -(|\ \beta\beta\alpha\ \rangle + e^{-i2\pi/3}|\ \alpha\beta\beta\ \rangle + e^{i2\pi/3}|\ \beta\alpha\beta\ \rangle)3^{-1/3} \quad (4)$$

E_b:

$$(|\alpha\alpha\beta\rangle + e^{i2\pi/3}|\beta\alpha\alpha\rangle + e^{-i2\pi/3}|\alpha\beta\alpha\rangle)3^{-1/3},\ -(|\ \beta\beta\alpha\ \rangle + e^{i2\pi/3}|\ \alpha\beta\beta\ \rangle + e^{-i2\pi/3}|\ \beta\alpha\beta\ \rangle)3^{-1/3} \quad (5)$$

In addition, we must consider the carbon spin states leading to a total of 16 states for the $^{13}CH_3$ moiety. Like Fig. 3, Fig. 4 displays the energy levels (panel a) and the possible relaxation pathways (panels b to d) for the methyl group between the populations of eigenstates. Again, transitions between spin manifolds of different symmetry are forbidden to first order. Hence, for the methyl group, a long-lived population imbalance between the A and E states can be created when overpopulating either of the manifolds.

Importantly, the relaxation pathway due to the DD CH-CH component is again asymmetric w.r.t. the vertical symmetry axis in Fig. 4. Hence, as explained

above, this pathway causes a conversion of proton polarization into carbon polarization of opposite sign. Another similarity to the CH_2 case is that relaxation of the A-E spin-state imbalance does not as efficiently produce $^{13}C_z$ magnetization as longitudinal ^1H magnetization.

The only marked difference between the methylene and methyl cases is that the HH-HH and CH-HH DD CCR components can cause a transition between the A and E manifolds, while no such transition between T and S can be observed in methylene groups. The internal methyl group rotation must be infinitely fast to establish a 'perfect' separation between the irreducible representations,[21] which is not the case in a typical methyl group.

Note that the representations in Fig. 3 and 4 are incomplete as they only show relaxation between populations without considering possible coherences. A detailed analysis of our simulations has revealed how these components, even if present, do not produce a critical contribution to the overall relaxation. Therefore, we decided to omit them in the graphical visualization. Furthermore, the matrix elements with values below 1% of the highest relaxation contribution are omitted for clarity.

DISCUSSION

The data in Fig. 2 demonstrate that the protonated ^{13}C nuclei of methanol, pyruvate, and EG are strongly affected during sample transport, as attested by the fact that their signals have opposite signs. In contrast, the deuterated $^{13}CD_2$ nuclei in glycerol-d_8, as well as the quaternary $^{13}C1$ signal of pyruvate, display the expected results, *i.e.*, strong signal enhancements with signs that correspond to the polarization built up by DNP before dissolution. In the following, we demonstrate that these observations can be explained by $^1H \rightarrow {}^{13}C$ cross-correlated cross-relaxation (CCR) during sample transfer.

Figure 5a shows the positive signal intensities of the methanol $^{13}CH_3$ quadruplet after negative DNP and transfer to the NMR spectrometer for detection. After injection (at t = 0), the four lines of the $^{13}CH_3$ quadruplet have been fitted to intensity ratios of (+0.8 : +3.3 : +3.1 : +1.0) $\rightleftharpoons$ 0.08 that depart from the usual +1 : +3 : +3 : +1 ratios observed in thermal equilibrium. This can be understood when assuming that the spin state of a methyl group immediately after dissolution, *i.e.*, before passage through the low-field region, comprises a linear combination of different distributions of populations. Three types were found important: ^1H_Z longitudinal magnetization of all three methyl protons, $^{13}C_Z$ longitudinal magnetization, and an A-E imbalance.

Although our theoretical considerations outlined above show that the influence of A-E imbalances on CCR is relatively weak compared to that of longitudinal magnetization, such population imbalances are often encountered in DDNP experiments involving methyl groups[14, 21, 38-41]. The overpopulation of either the lowest (after positive DNP) or highest (after negative DNP) energy levels in the solid-state before dissolution necessarily leads to a population imbalance between the A and E symmetry manifolds. E-state overpopulation is expected after negative DNP of methyl groups undergoing rapid proton tunneling, as the latter results in an energy increase of the E-states relative to the A-states. A detailed explanation can be found in references [21, 42]. A-state overpopulation is expected for all cases of positive DNP and negative DNP in slowly tunneling systems.[38] Fig. 5b illustrates the population differences between the various spin levels for the A-E imbalance, the longitudinal ^1H_Z and $^{13}C_Z$ magnetizations, as well as a typical linear combination. Note that such initial populations are expected for DNP using the nitroxide TEMPOL, since this polarization agent can polarize both protons and carbon-13 nuclei simultaneously, albeit with lesser efficiency for the latter, unless cross-polarization techniques are used.[43]

Many experiments have been performed with pyruvate without observing the effect reported in this work. This can be ascribed to the fact that such experiments used narrow-band radicals such as trityls to hyperpolarize the carbon-13 spins in the context of clinical or preclinical hyperpolarized MRI.[24, 27] Since these radicals do not hyperpolarize proton spins efficiently, the phenomenon described here is not expected in these experiments. However, as other types of radicals that polarize both proton and carbon spins are more common for applications in physical chemistry,[44-45] we expect more reports of such effect in this context.

The NMR signal phase. To model the signal amplitudes and their evolution as a function of time after dissolution, we employed the SpinDynamica[35] software package and let the spin system evolve under the total relaxation superoperator, including CSA, DD, DD-CSA, and random field relaxation. The Supporting Information contains detailed codes and information about these simulations. We could reproduce the experimental signal intensities when considering an initial distribution ^1H_z : $^{13}C_z$: A-E = -1: -0.01 : 3 directly after dissolution (at t = -12 s). This combination of populations is transformed into a distribution with an opposite sign for $^{13}C_z$ at t = 0 s.

Fig. 5a shows how the different components of the identified population combination contribute to the experimentally observed signal at the time of detection, *i.e.*, after the transfer during which CCR acts.

While the A-E and T-S imbalances lead to a ^{13}C signal in anti-phase with respect to the ^{1}H spins and to the inversion of two lines, relaxation of longitudinal $^{1}H_z$ magnetization leads to an inversion of all four lines, and longitudinal $^{13}C_z$ magnetization leads to the expected non-inverted line shape. Only combining all three contributions enabled us to reproduce the experimentally observed line shape, an inverted multiplet with asymmetric line intensities.

Note that the magnetization types indicated in Fig 5. correspond to the magnetization produced in a solid by DNP, while the detected multiplets stem from superpositions of in-phase and anti-phase contributions. Indeed, CCR the three produced magnetization types creates C_z, $C_zH_z^{(1)}$, $C_zH_z^{(1)}H_z^{(2)}$,as well as $C_zH_z^{(1)}H_z^{(2)}H_z^{(3)}$ type spin states, which upon applying a detection pulse on the carbon channel lead to anti-phase and in-phase coherences.

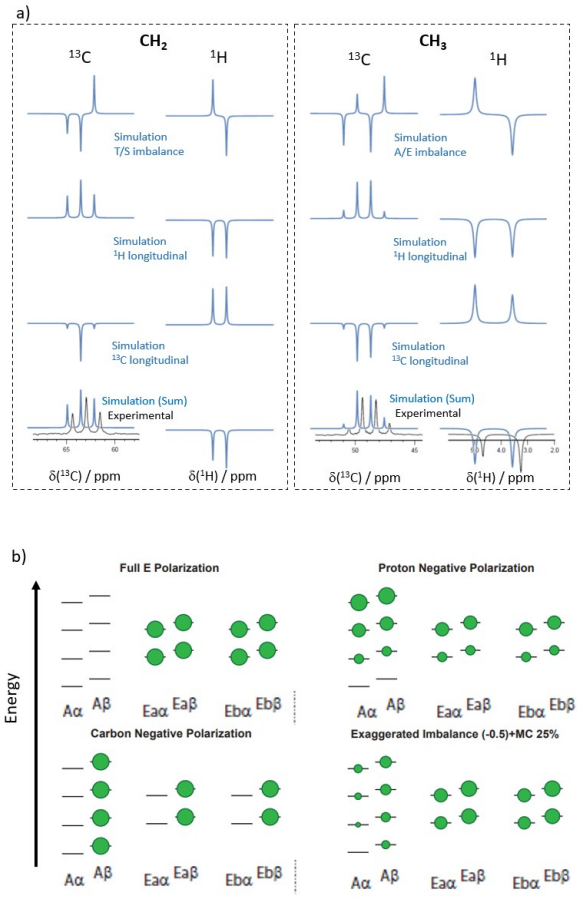

Figure 5. Contributions of different spin states to the experimentally detected ^{13}C spectrum (corresponding to t = 0 in Figs 6 and 7) due to cross-correlated cross-relaxation. Both CH_2 and CH_3 groups could be simulated by combining longitudinal $^{1}H_z$ and $^{13}C_z$ magnetizations with population imbalances between the respective irreducible representations (T-S and A-E, respectively). The former two contributions lead to roughly symmetric multiplets, while the population imbalances lead to asymmetric multiplets. Their superposition agrees with the observed signals. Note that the indicated magnetization types correspond to population distributions produced in the solid by DNP, while the detected multiplets stem from superpositions of in-phase and anti-phase coherences after dissolution. b) Sketch of the population distributions for the methyl group used to simulate the data in panel a). The sizes of the green spheres are proportional to the populations of the energy levels. The bottom right panel shows a combination of an A-E imbalance (with over-populated E-states), negative $^{1}H_z$ and negative $^{13}C_z$ polarizations. For visibility, the contributions of the A-E imbalance and the $^{13}C_z$ polarization have been exaggerated. The representation of the states used in the simulations can be found in the Supporting Information.

In Figure 6a, it can be seen that the aforementioned population distribution enabled simulations of line amplitudes for the ^{13}C quartet that match the experimentally observed ones well throughout the entire detection period (*i.e.*, for $t > 0$). In other words, not only the static spectrum at the time of injection could be reproduced, but also its evolution. We used a static magnetic field of 11.7 T for the simulations and a relaxation superperator as shown in Fig. 4. All other details on the simulation (coupling constants, Hamiltonians, etc.) can be found in the Supporting Information. Note that the signal detected experimentally upon arrival of the dissolved, hyperpolarized sample in the NMR spectrometer corresponds to t = 0 s in the simulations in Figure 6a. In other words, the simulations assumed an initial distribution at t = -12 s, such that t = 0 coincides with the onset of the experimental NMR detection. In this manner, the simulations reproduce the time evolutions of the experimental signal amplitudes.

The theoretical considerations in Fig. 3 and 4 already showed that DD CCR involving both, carbon and proton spins, is responsible for the inversion of the signal. This can be corroborated by our simulations. When the DD relaxation mechanism is removed from the relaxation superoperator, the inversion of magnetization is canceled (Fig. S1-S3 of the Supporting Information). Canceling any other relaxation mechanism changes the computed line shapes and time dependence, but the signal inversion remains. Hence, it can be inferred that cross-correlated relaxation effects, in particular DD CCR, lead to an inversion of the $^{13}C_z$ magnetization, which converts the A-E imbalance and the positive longitudinal ^{1}H magnetization into negative $^{13}C_z$ polarization.

In other words, by selectively discarding various contributions from the relaxation superoperator, we found that DD CH-CH relaxation is responsible for converting the largest share of $^{1}H_z$ into $^{13}C_z$ magnetization (Fig. S1-S3 of the SI). Werbelow and Grant already reported the influence of non-equilibrium $^{1}H_z$ magnetization on $^{13}C_z$ in their seminal work on relaxation.[46] However, the effects were relatively weak as only thermal equilibrium magnetization was involved, in stark contrast to the hyperpolarized case at hand. It should be noted that CSA relaxation can also invert smaller amounts of the $^{13}C_z$ order, although this con-

tribution is expected to decrease (or even to be negligible in ZULF NMR[47]).

Complementarily Fig. 6b shows the mono-exponential behavior (dotted line) of the (positive) observed $^{1}H_Z$ magnetization confirming the high ^{1}H polarization underlying our simulations. The data stems mostly from $^{12}CH_3$ methyl groups since the sample had natural isotopic ^{13}C abundance. However, simulations for $^{13}CH_3$ methyl groups (solid line) obtained with the same parameters used to fit the ^{13}C data result in a bi-exponential behavior of the (*negative*) ^{1}H magnetization. Fig. 6c represents the population distributions used for simulation.

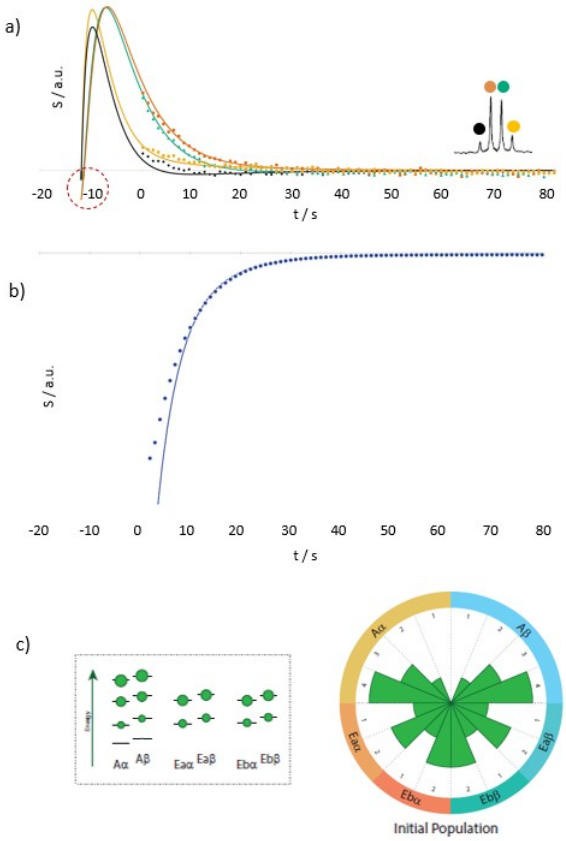

Figure 6. a) ^{13}C decay curves of hyperpolarized methanol after injection into the NMR spectrometer (dotted curves). The color code indicates the different lines of the methanol quartet as indicated in the insert. The solid lines stem from a simulation using a starting polarization consisting of an A-E imbalance and longitudinal proton and longitudinal carbon magnetizations as described in the main text. NMR observation started at time point $t = 0$. Extrapolations of populations before NMR detection are expressed by $t < 0$. b) Mono-exponential decay (dotted line) of the ^{1}H signal of $^{12}CH_3$ in natural abundance methanol detected in parallel to the $^{13}CH_3$ decay curves shown in panel a. c) Sketch of the population distributions of the methyl group used to simulate the data in panels a) and b). The sizes of the green spheres are proportional to the populations of the energy levels. The right panel visualizes the populations in the circular representation used in the Theory section.

For the $^{13}CH_2$ signals of EG, similar simulations as for the methyl groups could reproduce the experimental observations. Only the A-E imbalance of CH_3 groups had to be replaced by the triplet-singlet (T-S) imbalance of the CH_2 groups.[22] Hence, the behavior of both methyl and methylene groups can be explained equivalently by CCR effects. For methylene, a starting magnetization $^{1}H_Z : {}^{13}C_Z : \text{T-S} = 1 : 0.01 : 0.5$ was found to provide a good match between simulated and experimental data (Fig. 7).

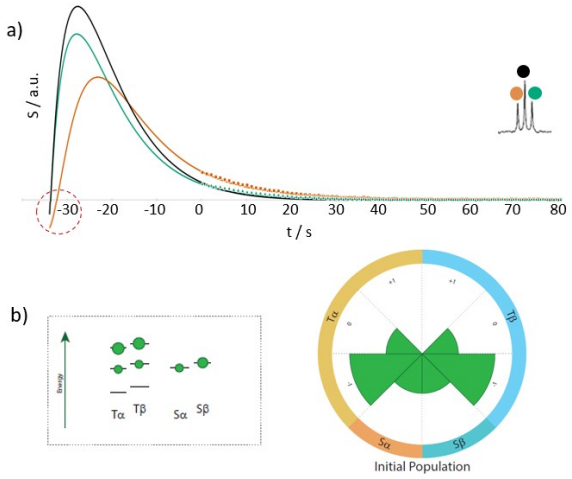

Figure 7. Build-up and decay curves of $^{13}CH_2$ groups in hyperpolarized EG after transfer to the NMR spectrometer (dotted curves). The color code indicates the three lines of the $^{13}CH_2$ triplet as indicated in the insert. The solid lines stem from a simulation using a starting polarization consisting of a triplet-singlet imbalance T-S, and longitudinal proton and longitudinal carbon magnetizations as described in the main text. NMR observation started at time point $t = 0$. Extrapolations to the time before NMR detection are represented by $t < 0$. b) Sketch of the population distributions of the methyl group used to simulate the data in panel a). The sizes of the green spheres are proportional to the populations of the energy levels. The right panel visualizes the populations in the circular representation used in the Theory section.

It should be noted that the signals of deuterated glycerol are not inverted for two reasons. First, the hyperpolarization levels achieved for the deuterons are not as high as those achieved for protons and decay much faster under quadrupolar relaxation.[39-40] Secondly, the CCR processes leading to signal inversion observed for protons are not efficient in the case of deuterons.[35-36] In contrast, the signal of the quaternary ^{13}C nucleus in pyruvate-C1 is not inverted as all neighboring nuclei to the detected ^{13}C are largely NMR inactive.

The rate of relaxation. In our simulations, relatively long intervals $t = 12$ s and 34 s between the start of the trajectory and the time point when the system reaches the intensity ratio of the observed multiplets have been assumed to describe the methyl and methylene groups, respectively. However, in our DDNP experiments, the sample transfer took only 5 s. The passage through low magnetic fields was much shorter. Hence, relaxation processes must become faster during sample transfer to account for our ob-

servations. However, semi-classical calculations using RedKite[36] did not show a strong field dependence of the relaxation rates in an isolated methyl group.

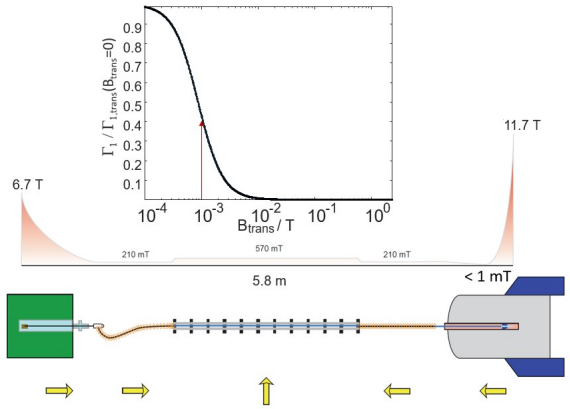

Figure 8. Sketch of the magnetic fields encountered during sample transport. The yellow arrows mark the direction of the fields. Within the magnetic tunnel, a field of B_0 >570 mT is achieved by a four-element Halbach array. Between the polarizer/NMR spectrometer and the tunnel, pulsed solenoids produced a magnetic field of ca. B_0 = 210 mT. Between the solenoid outlet and the Bruker 'Ultra-Shielded' NMR spectrometer, the field dropped to B_0 < 1 mT. The insert shows how the longitudinal paramagnetic relaxation enhancement due to the 0.36 mM TEMPOL in the solution is accelerated due to the low-field passage (see main text). Indeed, at a field of 1 mT, the relaxation rate increases rapidly compared to the 11.7 T within the NMR spectrometer.

In contrast, to reproduce the experimentally observed behavior, the influence of free radicals in the solution during sample transfer had to be considered. Indeed, Jannin and co-workers have shown[48] that ^{13}C relaxation in the presence of TEMPOL radicals is significantly accelerated at low magnetic fields. More importantly, for the present context, Kiryutin and co-workers[31] have shown that ^{1}H relaxation rates accelerate by order of magnitude due to low-field passage in the presence of TEMPOL. Hence, the reduced time needed for the signal inversion of the protonated species might be accounted for by faster, paramagnetically induced relaxation during sample transfer in our DDNP experiments. This assumption is supported by the works of Ghose et al.[49], Boisbouvier et al.[50], Bertini et al.[51-52], and Madhu et al.[53]. These authors showed that interference between paramagnetic relaxation enhancement and heteronuclear dipole-dipole relaxation impacts the relaxation properties of paramagnetic systems by enhancing DD relaxation and creating multi-spin order.[53] The latter can lead to magnetization transfers between different nuclei. Importantly, this effect is strongly field-dependent.[53]

A simulation of the field dependence of solvent paramagnetic relaxation enhancements (sPRE) further supports that strong relaxation enhancements can be induced by co-dissolved radicals. Fig. 8 shows a sketch of the different magnetic fields encountered during the transfer in the Vienna laboratory (see also Fig. S4). Between the outlet of the tunnel and the entrance to the NMR spectrometer bore, the transient magnetic field drops to less than 1 mT. The insert shows how the longitudinal proton relaxation rate due to dissolved TEMPOL Γ_1 (blue curve) changes with the magnetic field. The curve was calculated following the spectral density function for sPRE by Okuno and co-workers[54]. Details on the calculations can be found in the Supporting Information. The black arrow indicates the transiently encountered magnetic field of 1 mT. The sPRE dramatically boosts relaxation rates during low-field passage. Therefore, the low-field passage likely increases relaxation rates significantly at magnetic fields encountered during the sample transfer. Hence, the discrepancy between 5 s experimental transfer times and the >10 s theoretically calculated delays can possibly be accounted for by paramagnetically accelerated DD relaxation during sample transfer.

CONCLUSIONS

In conclusion, we show that different relaxation mechanisms taking place during sample transfer can drastically affect the outcome of dissolution DNP experiments. NMR spectra can be inverted, and hyperpolarized spin states can be effectively depleted or unexpectedly enhanced.

These effects are amplified by so-called "ultra-shielded" NMR magnets that provide only minimal stray fields, which can accelerate relaxation between hyperpolarized protons and carbon spins when paramagnetic polarization agents remain in the solution after dissolution. To avoid the effect of cross-relaxation in ^{13}C NMR spectra, one may employ deuterated molecules. Alternatively, a magnetic tunnel that guides the sample into the bore of the NMR spectrometer can slow down relaxation effects.[30]

Besides, we show how simulations and 'backpropagation' of the experimental time dependence can be employed to determine the state of the spin system back to the moment of dissolution.

The growing popularity of DDNP in combination with novel magnet shielding technologies will likely lead to more observations of signal inversion effects, and the presented contribution can help identify and quantify these phenomena.

Supporting Information

The Supporting Information is available free of charge at

Simulation of CH_3 group relaxation with neglected mechanisms, simulation of CH_3 group relaxation with different A-E imbalance, representation of the population used for simulation, ^{1}H T_1 relaxation with various field variation, simulation parameter, SpinDynam-

ica code for CH_3 and CH_2 group relaxation, calculation of sPRE.

Acknowledgments

The authors acknowledge support by the NMR core facility of the Faculty of Chemistry, University Vienna. The project leading to this application received funding from the European Research Council (ERC) under the European Union's Horizon 2020 research and innovation programme (grant agreements 801936 and 339754). This project was further supported by an FWF stand-alone grant (no. P-33338 N). This work was further supported by the French CNRS.

Conflict of Interest

The authors declare no conflicts of interest.

Data Availability

All data are available under DOI 10.5281/zenodo.6580927.

Code Availability

All codes are available under DOI 10.5281/zenodo.6580927.

References

1. Kovtunov, K. V.; Pokochueva, E. V.; Salnikov, O. G.; Cousin, S. F.; Kurzbach, D.; Vuichoud, B.; Jannin, S.; Chekmenev, E. Y.; Goodson, B. M.; Barskiy, D. A.; et al, Hyperpolarized NMR Spectroscopy: d-DNP, PHIP, and SABRE Techniques. *Chem Asian J* **2018,** *13*(15), 1857-1871.
2. Nikolaou, P.; Goodson, B. M.; Chekmenev, E. Y., NMR hyperpolarization techniques for biomedicine. *Chemistry* **2015,** *21* (8), 3156-66.
3. Ardenkjaer-Larsen, J. H.; Fridlund, B.; Gram, A.; Hansson, G.; Hansson, L.; Lerche, M. H.; Servin, R.; Thaning, M.; Golman, K., Increase in signal-to-noise ratio of > 10,000 times in liquid-state NMR. *Proc Natl Acad Sci U S A* **2003,** *100* (18), 10158-63.
4. Jannin, S.; Dumez, J. N.; Giraudeau, P.; Kurzbach, D., Application and methodology of dissolution dynamic nuclear polarization in physical, chemical and biological contexts. *J Magn Reson* **2019,** *305*, 41-50.
5. Leggett, J.; Hunter, R.; Granwehr, J.; Panek, R.; Perez-Linde, A. J.; Horsewill, A. J.; McMaster, J.; Smith, G.; Kockenberger, W., A dedicated spectrometer for dissolution DNP NMR spectroscopy. *Phys Chem Chem Phys* **2010,** *12* (22), 5883-92.
6. Niedbalski, P.; Parish, C.; Kiswandhi, A.; Lumata, L., C-13 dynamic nuclear polarization using isotopically enriched 4-oxo-TEMPO free radicals. *Magn Reson Chem* **2016,** *54* (12), 962-967.
7. Ragavan, M.; Iconaru, L. I.; Park, C. G.; Kriwacki, R. W.; Hilty, C., Real-Time Analysis of Folding upon Binding of a Disordered Protein by Using Dissolution DNP NMR Spectroscopy. *Angew Chem Int Ed Engl* **2017,** *56* (25), 7070-7073.
8. Szekely, O.; Olsen, G. L.; Felli, I. C.; Frydman, L., High-resolution 2D NMR of disordered proteins enhanced by hyperpolarized water. *Anal Chem* **2018** *90*(10), 6169−6177.
9. Olsen, G. L.; Szekely, O.; Mateos, B.; Kaderavek, P.; Ferrage, F.; Konrat, R.; Pierattelli, R.; Felli, I. C.; Bodenhausen, G.; Kurzbach, D.; et al, Sensitivity-enhanced three-dimensional and carbon-detected two-dimensional NMR of proteins using hyperpolarized water. *J Biomol Nmr* **2020,** *74* (2-3), 161-171.
10. Kurzbach, D.; Canet, E.; Flamm, A. G.; Jhajharia, A.; Weber, E. M.; Konrat, R.; Bodenhausen, G., Investigation of Intrinsically Disordered Proteins through Exchange with Hyperpolarized Water. *Angew Chem Int Ed Engl* **2017,** *56* (1), 389-392.
11. Sadet, A.; Stavarache, C.; Bacalum, M.; Radu, M.; Bodenhausen, G.; Kurzbach, D.; Vasos, P. R., Hyperpolarized Water Enhances Two-Dimensional Proton NMR Correlations: A New Approach for Molecular Interactions. *J Am Chem Soc* **2019,** *141* (32), 12448-12452.
12. Mieville, P.; Jannin, S.; Helm, L.; Bodenhausen, G., Kinetics of Yttrium-Ligand Complexation Monitored Using Hyperpolarized Y-89 as a Model for Gadolinium in Contrast Agents. *Journal of the American Chemical Society* **2010,** *132* (14), 5006-+.
13. Kim, Y.; Liu, M. X.; Hilty, C., Parallelized Ligand Screening Using Dissolution Dynamic Nuclear Polarization. *Analytical Chemistry* **2016,** *88* (22), 11178-11183.
14. Kress, T.; Walrant, A.; Bodenhausen, G.; Kurzbach, D., Long-Lived States in Hyperpolarized Deuterated Methyl Groups Reveal Weak Binding of Small Molecules to Proteins. *Journal of Physical Chemistry Letters* **2019,** *10* (7), 1523-1529.

15. Dumez, J. N.; Milani, J.; Vuichoud, B.; Bornet, A.; Lalande-Martin, J.; Tea, I.; Yon, M.; Maucourt, M.; Deborde, C.; Moing, A.; et al, Hyperpolarized NMR of plant and cancer cell extracts at natural abundance. *Analyst* **2015,** *140* (17), 5860-5863.
16. Dey, A.; Charrier, B.; Martineau, E.; Deborde, C.; Gandriau, E.; Moing, A.; Jacob, D.; Eshchenko, D.; Schnell, M.; Melzi, R.; et al, Hyperpolarized NMR Metabolomics at Natural (13)C Abundance. *Anal Chem* **2020,** *92* (22), 14867-14871.
17. Miclet, E.; Abergel, D.; Bornet, A.; Milani, J.; Jannin, S.; Bodenhausen, G., Toward Quantitative Measurements of Enzyme Kinetics by Dissolution Dynamic Nuclear Polarization. *J Phys Chem Lett* **2014,** *5* (19), 3290-5.
18. Novakovic, M.; Olsen, G. L.; Pinter, G.; Hymon, D.; Furtig, B.; Schwalbe, H.; Frydman, L., A 300-fold enhancement of imino nucleic acid resonances by hyperpolarized water provides a new window for probing RNA refolding by 1D and 2D NMR. *Proc Natl Acad Sci U S A* **2020,** *117* (5), 2449-2455.
19. Boeg, P. A.; Duus, J. Ø.; Ardenkjær-Larsen, J. H.; Karlsson, M.; Mossin, S., Real-Time Detection of Intermediates in Rhodium-Catalyzed Hydrogenation of Alkynes and Alkenes by Dissolution DNP. *J. Chem. Phys. C* **2019,** *123*, 9949-9956.
20. Tayler, M. C.; Marco-Rius, I.; Kettunen, M. I.; Brindle, K. M.; Levitt, M. H.; Pileio, G., Direct enhancement of nuclear singlet order by dynamic nuclear polarization. *J Am Chem Soc* **2012,** *134* (18), 7668-71.
21. Dumez, J. N.; Hakansson, P.; Mamone, S.; Meier, B.; Stevanato, G.; Hill-Cousins, J. T.; Roy, S. S.; Brown, R. C.; Pileio, G.; Levitt, M. H., Theory of long-lived nuclear spin states in methyl groups and quantum-rotor induced polarisation. *J Chem Phys* **2015,** *142* (4), 044506.
22. Mammoli, D.; Vuichoud, B.; Bornet, A.; Milani, J.; Dumez, J. N.; Jannin, S.; Bodenhausen, G., Hyperpolarized para-Ethanol. *J Phys Chem B* **2015,** *119* (10), 4048-4052.
23. Nelson, S. J.; Vigneron, D.; Kurhanewicz, J.; Chen, A.; Bok, R.; Hurd, R., DNP-Hyperpolarized C Magnetic Resonance Metabolic Imaging for Cancer Applications. *Appl Magn Reson* **2008,** *34* (3-4), 533-544.
24. Nelson, S. J.; Kurhanewicz, J.; Vigneron, D. B.; Larson, P. E.; Harzstark, A. L.; Ferrone, M.; van Criekinge, M.; Chang, J. W.; Bok, R.; Park, I.; et al, Metabolic imaging of patients with prostate cancer using hyperpolarized [1-(1)(3)C]pyruvate. *Sci Transl Med* **2013,** *5* (198), 198ra108.
25. Eichhorn, T. R.; Takado, Y.; Salameh, N.; Capozzi, A.; Cheng, T.; Hyacinthe, J. N.; Mishkovsky, M.; Roussel, C.; Comment, A., Hyperpolarization without persistent radicals for in vivo real-time metabolic imaging. *Proc Natl Acad Sci U S A* **2013,** *110* (45), 18064-9.
26. Wilson, D. M.; Kurhanewicz, J., Hyperpolarized C-13 MR for Molecular Imaging of Prostate Cancer. *J Nucl Med* **2014,** *55* (10), 1567-1572.
27. Krajewski, M.; Wespi, P.; Busch, J.; Wissmann, L.; Kwiatkowski, G.; Steinhauser, J.; Batel, M.; Ernst, M.; Kozerke, S., A multisample dissolution dynamic nuclear polarization system for serial injections in small animals. *Magn Reson Med* **2017,** *77* (2), 904-910.
28. Ardenkjaer-Larsen, J. H.; Bowen, S.; Petersen, J. R.; Rybalko, O.; Vinding, M. S.; Ullisch, M.; Nielsen, N. C., Cryogen-free dissolution dynamic nuclear polarization polarizer operating at 3.35 T, 6.70 T, and 10.1 T. *Magn Reson Med* **2019,** *81* (3), 2184-2194.
29. Milani, J.; Vuichoud, B.; Bornet, A.; Mieville, P.; Mottier, R.; Jannin, S.; Bodenhausen, G., A magnetic tunnel to shelter hyperpolarized fluids. *Rev Sci Instrum* **2015,** *86* (2), 024101.
30. Kouřil, K.; Kouřilová, H.; Levitt, M. H.; Meier, B., Dissolution-Dynamic Nuclear Polarization with Rapid Transfer of a Polarized Solid. *Nat Commun* **2019,** *10*, 1733.
31. Kiryutin, A. S.; Rodin, B. A.; Yurkovskaya, A. V.; Ivanov, K. L.; Kurzbach, D.; Jannin, S.; Guarin, D.; Abergel, D.; Bodenhausen, G., Transport of hyperpolarized samples in dissolution-DNP experiments. *Phys Chem Chem Phys* **2019,** *21* (25), 13696-13705.
32. Kress, T.; Che, K.; Epasto, L. M.; Kozak, F.; Negroni, M.; Olsen, G. L.; Selimovic, A.; Kurzbach, D., A novel sample handling system for dissolution dynamic nuclear polarization experiments. *Magnetic Resonance* **2021,** *2*, 387-394.
33. Jannin, S.; Bornet, A.; Colombo, S.; Bodenhausen, G., Low-temperature cross polarization in view of enhancing dissolution Dynamic

Nuclear Polarization in NMR. *Chem Phys Lett* **2011,** *517* (4-6), 234-236.
34. Bornet, A.; Pinon, A.; Jhajharia, A.; Baudin, M.; Ji, X.; Emsley, L.; Bodenhausen, G.; Ardenkjaer-Larsen, J. H.; Jannin, S., Microwave-gated dynamic nuclear polarization. *Phys Chem Chem Phys* **2016,** *18* (44), 30530-30535.
35. Bengs, C.; Levitt, M. H., SpinDynamica: Symbolic and numerical magnetic resonance in a Mathematica environment. *Magn Reson Chem* **2018,** 56(6), 374–414.
36. Bolik-Coulon, N.; Kaderavek, P.; Pelupessy, P.; Dumez, J. N.; Ferrage, F.; Cousin, S. F., Theoretical and computational framework for the analysis of the relaxation properties of arbitrary spin systems. Application to high-resolution relaxometry. *J Magn Reson* **2020,** *313*, 106718.
37. Carravetta, M.; Johannessen, O. G.; Levitt, M. H., Beyond the T1 limit: singlet nuclear spin states in low magnetic fields. *Phys Rev Lett* **2004,** *92* (15), 153003.
38. Meier, B.; Dumez, J. N.; Stevanato, G.; Hill-Cousins, J. T.; Roy, S. S.; Hakansson, P.; Mamone, S.; Brown, R. C.; Pileio, G.; Levitt, M. H., Long-lived nuclear spin states in methyl groups and quantum-rotor-induced polarization. *J Am Chem Soc* **2013,** *135* (50), 18746-9.
39. Ivanov, K. L.; Kress, T.; Guarin, D.; Baudin, M.; Abergel, D.; Bodenhausen, G.; Kurzbach, D., Relaxation of long-lived modes in NMR of deuterated methyl groups. *J. Chem. Phys.* **2018,** *149* (5), 054202.
40. Jhajharia, A.; Weber, E. M.; Kempf, J. G.; Abergel, D.; Bodenhausen, G.; Kurzbach, D., Communication: Dissolution DNP reveals a long-lived deuterium spin state imbalance in methyl groups. *J Chem Phys* **2017,** *146* (4), 041101.
41. Kurzbach, D.; Weber, E. M. M.; Jhajharia, A.; Cousin, S. F.; Sadet, A.; Marhabaie, S.; Canet, E.; Birlirakis, N.; Milani, J.; Jannin, S.; et al, D., Dissolution Dynamic Nuclear Polarization of Deuterated Molecules Enhanced by Cross-Polarization *J. Chem. Phys.* **2016,** *145*, 194203.
42. Dumez, J. N.; Vuichoud, B.; Mammoli, D.; Bornet, A.; Pinon, A. C.; Stevanato, G.; Meier, B.; Bodenhausen, G.; Jannin, S.; Levitt, M. H., Dynamic Nuclear Polarization of Long-Lived Nuclear Spin States in Methyl Groups. *J Phys Chem Lett* **2017,** *8* (15), 3549-3555.
43. Vuichoud, B.; Milani, J.; Bornet, A.; Melzi, R.; Jannin, S.; Bodenhausen, G., Hyperpolarization of deuterated metabolites via remote cross-polarization and dissolution dynamic nuclear polarization. *J Phys Chem B* **2014,** *118* (5), 1411-5.
44. Gajan, D.; Bornet, A.; Vuichoud, B.; Milani, J.; Melzi, R.; Kalkeren, H. A. v.; Veyre, L.; Thieuleux, C.; Conley, M. P.; Grüning, W. R.; et al, Hybrid polarizing solids for pure hyperpolarized liquids through dissolution dynamic nuclear polarization. *Proc. Natl. Acad. Sci.* **2014,** *111*, 14693-14697.
45. Lipso, K. W.; Bowen, S.; Rybalko, O.; Ardenkjaer-Larsen, J. H., Large dose hyperpolarized water with dissolution-DNP at high magnetic field. *J Magn Reson* **2017,** *274*, 65-72.
46. Werbelow, L. G.; Grant, D. M., Intramolecular Dipolar Relaxation in Multispin Systems. In *Advances in Magnetic Resonance*, Academic Press: New York, 1977; Vol. 9.
47. Tayler, M. C. D.; Theis, T.; Sjolander, T. F.; Blanchard, J. W.; Kentner, A.; Pustelny, S.; Pines, A.; Budker, D., Invited Review Article: Instrumentation for nuclear magnetic resonance in zero and ultralow magnetic field. *Rev Sci Instrum* **2017,** *88* (9), 091101.
48. Mieville, P.; Jannin, S.; Bodenhausen, G., Relaxometry of insensitive nuclei: optimizing dissolution dynamic nuclear polarization. *J Magn Reson* **2011,** *210* (1), 137-40.
49. Ghose, R.; Prestegard, J. H., Electron spin-nuclear spin cross-correlation effects on multiplet splittings in paramagnetic proteins. *J Magn Reson* **1997,** *128* (2), 138-43.
50. Boisbouvier, J.; Gans, P.; Blackledge, M.; Brutscher, B.; Marion, D., Long-range structural information in NMR studies of paramagnetic molecules from electron spin-nuclear spin cross-correlated relaxation. *Journal of the American Chemical Society* **1999,** *121* (33), 7700-7701.
51. Bertini, I.; Cavallaro, G.; Cosenza, M.; Kummerle, R.; Luchinat, C.; Piccioli, M.; Poggi, L., Cross correlation rates between Curie spin and dipole-dipole relaxation in paramagnetic proteins: the case of cerium substituted calbindin D9k. *J Biomol Nmr* **2002,** *23* (2), 115-25.
52. Bertini, I.; Luchinat, C.; Tarchi, D., Are True Scalar Proton Proton Connectivities Ever Measured in Cosy Spectra of Paramagnetic

Macromolecules. *Chem Phys Lett* **1993,** *203* (5-6), 445-449.
53. Madhu, P. K.; Mandal, P. K.; Muller, N., Cross-correlation effects involving curie spin relaxation in methyl groups. *J Magn Reson* **2002,** *155* (1), 29-38.
54. Okuno, Y.; Szabo, A.; Clore, G. M., Quantitative Interpretation of Solvent Paramagnetic Relaxation for Probing Protein-Cosolute Interactions. *J Am Chem Soc* **2020,** *142* (18), 8281-8290.

TOC Graphic